Impedance-Based High-Frequency Resonance Analysis of DFIG System in Weak Grids

Yipeng Song, Xiongfei Wang, *Member, IEEE*, and Frede Blaabjerg, *Fellow, IEEE*

***Abstract*—The impedance-based model of doubly fed induction generator (DFIG) systems, including the rotor part (rotor side converter (RSC) and induction machine), and the grid part (grid side converter (GSC) and its output filter), has been developed for analysis and mitigation of the subsynchronous resonance (SSR). However, the high-frequency resonance (HFR) of DFIG systems due to the impedance interaction between the DFIG system and parallel compensated weak network is often overlooked. This paper, thus, investigates the impedance characteristics of DFIG systems for the analysis of HFR. The influences of the rotor speed variation, the machine mutual inductance and the digital control delay are evaluated. Two resonances phenomena are revealed, i.e., 1) the series HFR between the DFIG system and weak power grid; 2) the parallel HFR between the rotor part and the grid part of DFIG system. The impedance modeling of DFIG system and weak grid network, as well as the series HFR between DFIG system and parallel compensated weak network has been validated by experimental results.**

***Index Terms*—DFIG system impedance modeling, high-frequency resonance (HFR), weak network impedance modeling.**

I. Introduction

WIND power generation based on the doubly fed induction generator (DFIG) system has gained an increasing popularity [1]–[4] in the past years. It has a smaller power rating requirement for power electronics devices, i.e., around 30% of the generator rating, variable speed, and flexible power control capabilities, thus leading to the lower converter cost and power losses compared with the fixed-speed induction generators or synchronous generators with full-scale converters.

In the previous discussions [3]–[8] during the past few years, it is always assumed that the DFIG system is connected to the large scale stiff grid with its impedance small enough to be neglected. As a consequence, the impedance interaction between the DFIG system and the power grid does not exist, and the resonance is always overlooked. Nevertheless, as the distributed renewable power generation units and loads are increasingly installed in the weak and standalone network, its network impedance is comparatively much larger than that of the stiff grid, thus the impedance of the weak network deserves careful consideration.

Manuscript received December 30, 2015; revised March 30, 2016 and May 23, 2016; accepted June 20, 2016. Date of publication June 23, 2016; date of current version February 2, 2017. Recommended for publication by Associate Editor B. Wang.

The authors are with the Department of Energy Technology, Aalborg University, Aalborg 9220, Denmark (e-mail: yis@et.aau.dk; xwa@et.aau.dk; fbl@et.aau.dk).

Color versions of one or more of the figures in this paper are available online at http://ieeexplore.ieee.org.

Digital Object Identifier 10.1109/TPEL.2016.2584118

There are several papers investigating the performance of the DFIG system connected to the weak network with large impedance. The subsynchronous resonance (SSR) phenomenon [9]–[15] has been investigated under the circumstance that the DFIG system is radially connected to the power grid through long distant transmission cables, thus the series compensated capacitance is adopted to reduce the electric equivalent inductance of the transmission cables. Therefore, the impedance interaction between the DFIG system and the series compensated weak network requires serious considerations. The SSR between the DFIG system and the series compensated weak network has been well investigated on the basis of impedance modeling of DFIG machine and rotor side converter (RSC) as well as grid side converter (GSC) and its output filter in [9]–[15]. The harmonic linearization method is employed to obtain the positive and negative impedance sequence of the DFIG system in [9]–[11], and the influence of PI controller parameters in the rotor current closed-loop control and phase locked loop control on the SSR is studied, and the DFIG SSR under the different rotor speed is investigated too. Moreover, the overall equivalent circuit modeling of the DFIG system and weak grid network is reported in [12], and it is demonstrated that the interaction between the electric network and the converter controller is a leading cause of SSR. The Thyristor-Controlled Series Capacitor (TCSC) is reported in [13] to detect SSR in Type-3 wind farms, and it is found that DFIG RSC current control does not contribute to SSR instability under the TCSC compensation. The design of the auxiliary SSR damping controller and selection of control variables in the DFIG converters are explored in [14] in order to effectively mitigate the SSR.

However, it should be pointed out that in the previous DFIG impedance modeling literatures [9]–[15], the main focus is to theoretically explain the SSR (which is lower than fundamental frequency 50 Hz) between the DFIG system and the series compensated weak grids, while the high-frequency resonance (HFR), which is typically higher than 1 kHz, has not been addressed yet.

For the grid connected converter, the HFR has been well analyzed in the previous research [16]–[31]. The HFR between the grid connected converter and the RL weak network has been analyzed in [16]–[24]. The converter with series *LC* filter, rather than the traditional LCL filter, is studied in [17] to analyze the resonance. Moreover, the coupling between two converters connected to the same point of common coupling (PCC) or different point of coupling via nonideal grid is discussed in [25], and the bifurcation boundaries are also derived.

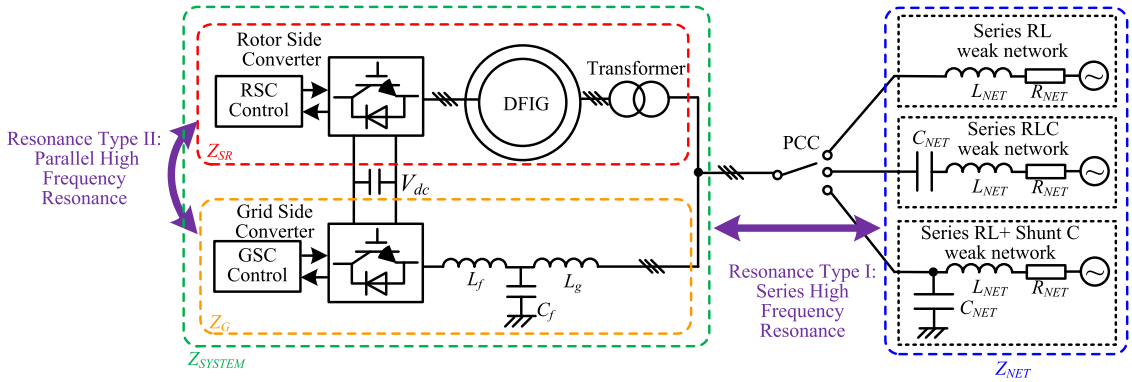

Fig. 1. Configuration diagram of the DFIG system and weak network.

Since the converter control parameters may influence its stability, the systematic design method of the controller parameter is given based on the chosen LCL filter resonance frequency in [26], [28], and [30]. The passivity-based technique is developed in [27] to assess the interconnection stability of voltage source converter through its input admittance. The digital control time delay, which may jeopardize the performance of the introduced virtual resistance, is reduced in [29], thus the virtual impedance can exhibit more like a resistor in a wider frequency range, ensuring high robustness against the grid-impedance variation.

It should be noted that the grid network consisting of resistor inductor capacitor (RLC) in series, that is series compensated weak network is taken into consideration in the DFIG SSR in [9]–[15], while the other types of network configurations, e.g., series RL and series RL + shunt C, that is parallel compensated weak network, are not under discussion in DFIG SSR analysis, but only discussed in the case of grid connected converter in [16]–[31]. As the off-shore wind farms [32]–[33] that contain large numbers of wind turbines continue to develop, the weak network with parallel compensated capacitance also occurs due to the requirement of reactive power compensation. Moreover, for the case of cable-based [34] wind power plants, the parasite capacitance between the cable and ground is inevitable, which also contributes to the parallel compensated weak network. Therefore, it is believed that the HFR due to the impedance interaction between the DFIG system and the parallel compensated weak network is worth investigating.

In this paper, the impedance modeling of the DFIG rotor part (machine and RSC) and the grid part (GSC and LCL filter) are established first as a foundation for resonance analysis, and the DFIG system impedance, including these two impedance parts in parallel, is given in Section II. Note that, in the previous analysis on SSR, the dc-link voltage closed-loop control and grid synchronization are taken into consideration since their dynamic response time is close to the SSR frequency, which is lower than the fundamental frequency. However, the HFR discussed in this paper has much higher frequency (typically around 1–2 kHz), thus the dc-link voltage closed-loop control and the grid synchronization are neglected in this paper due to their comparatively slower dynamic response. The series HFR between DFIG system and weak network is investigated under three different kinds of network configuration, i.e.: 1) series RL; 2) series RLC (series compensated weak network); and 3) series RL + shunt C (parallel compensated weak network) in Section III, and when the most popular network configuration of the series RL + shunt C is studied, the nonresonance stable range, critical but still stable range, as well as the resonance range are all analyzed in detail. The parallel HFR between DFIG rotor part and grid part is also analyzed in Section IV. The DFIG system impedance modeling and HFR are validated by experimental results in Section V. Finally, the conclusions are given in Section VI.

TABLE I
PARAMETERS OF RSC, DFIG MACHINE, GSC, AND LCL FILTER

L_g	7 mH	L_f	11 mH
C_f	6.6 μF	L_m	79.3 mH
$L_{\sigma s}$	3.44 mH	$L_{\sigma r}$	5.16 mH
R_s	0.44 Ω	R_r	0.64 Ω
K_{prsc}	8	K_{irsc}	16
K_{pgsc}	8	K_{igsc}	16
ω_r	0.8 p.u.	T_d	1.5e-4 s
f_s	10 kHz	f_{sw}	5 kHz

II. IMPEDANCE MODELING OF DFIG SYSTEM

For the purpose of explicitly explaining the DFIG system HFR, the general description of the DFIG system and weak network configuration is first presented. Unlike the previous modeling adopting L filter in GSC during the discussion of SSR [9]–[15], the LCL filter is implemented in this paper, thus it is essential to rebuild the DFIG system impedance modeling.

A. System Description

Fig. 1 shows the configuration diagram of the DFIG system and weak grid, the parameters of the DFIG system are available in Table I. As it can be seen, the RSC controls the rotor voltage to implement the DFIG machine stator output active and reactive power, GSC is responsible for providing stable dc-link voltage for the RSC, and unlike the previous works [9]–[12] adopting L filter, the GSC in this paper adopts the LCL filter due to better switching frequency harmonic filtering performance. For the purpose of preventing grid connection inrush and inner system current circulation, a transformer is connected between DFIG

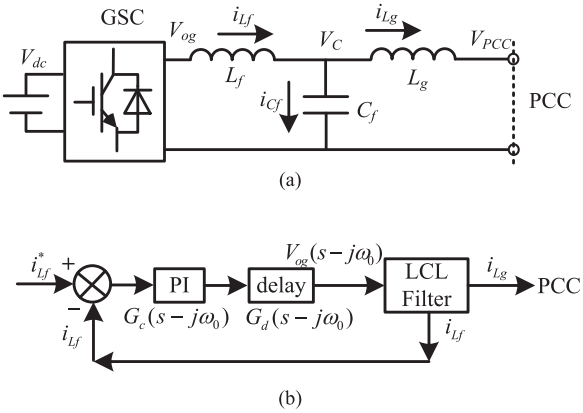

Fig. 2. Circuit and closed-loop control diagram of GSC with LCL filter.

stator winding and PCC, note that the transformer does not change the voltage level of primary side and secondary side, thus the transformer will be neglected during the impedance modeling in following sections.

As for the weak grid network, there are three kinds of different configurations as shown in Fig. 1, i.e., series RL network, series RLC network (series compensated weak network) and series RL + shunt C network (parallel compensated weak network), all three kinds of weak networks can be connected to the PCC.

Obviously, based on the configuration of DFIG system and weak networks, there are two different kinds of possible HFR.

1) When the weak network behaves capacitive (which will be analyzed in the following), while the DFIG system behaves inductive, then it is very likely for the series HFR to occur between DFIG system and weak grid network.
2) On the other hand, due to the adoption of LCL filter, the grid side of DFIG system will behave as capacitive unit within certain specific frequency range (which will be analyzed in the following), while the rotor part of DFIG system will maintain as an inductive unit, as a result the parallel HFR is likely to happen between rotor part and grid part within the DFIG system itself.

The following of this paper will theoretically analyze these two kinds of parallel and series HFR based on impedance modeling results.

B. GSC and LCL Filter Impedance Modeling

The impedance modeling of LCL filter based grid-connected converter has been well investigated in [22], since the DFIG GSC and LCL filter has the same configuration as the grid-connected converter, the impedance modeling results in [22] can be directly used here. For the sake of simplicity and clear explanation, the modeling result of GSC and LCL filter is mentioned in this section.

It can be seen from Fig. 2(a) that the GSC adopts the LCL filter due to better filtering of the switching harmonics. According to the current control block diagram in Fig. 2(b), the GSC control output voltage $V_{\rm og}$ can be presented as follows:

$$V_{\rm og}(s-j\omega_0) = (i^*_{\rm Lf} - i_{\rm Lf})\, G_c(s-j\omega_0) G_d(s-j\omega_0) \quad (1)$$

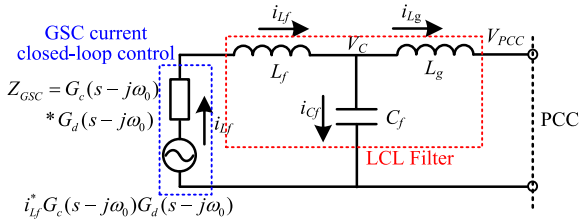

Fig. 3. Comprehensive circuit of GSC and LCL filter from Fig. 2.

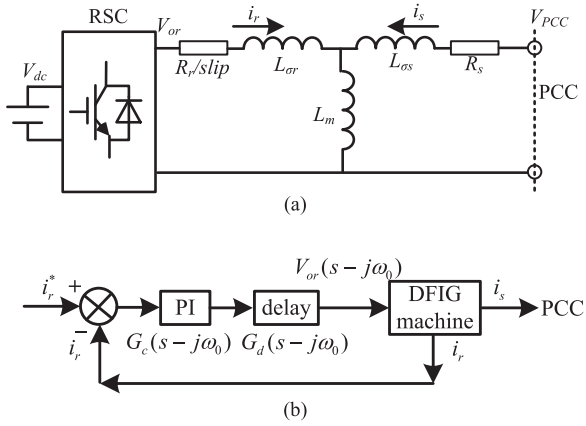

Fig. 4. Circuit and closed-loop control diagram of RSC and DFIG machine.

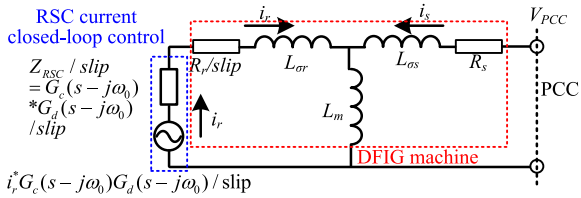

Fig. 5. Comprehensive circuit of RSC and DFIG machine from Fig. 3.

where $G_c(s-j\omega_0)$ is the PI current controller containing proportional part $K_{\rm pgsc}$ and integral part $K_{\rm igsc}/(s-j\omega_0)$, the parameters of $K_{\rm pgsc}$ and $K_{\rm igsc}$ can be found in Table I. $G_d(s-j\omega_0)$ is the digital control delay of 1.5 sample period. It needs to be pointed out that ω_0 is the grid network fundamental component angular speed of 100π rad/s, the introduction of ω_0 is due to the reference frame rotation from the stationary frame to the synchronous frame where the PI closed-loop current regulation is implemented.

The GSC control has an outer control loop of the dc-link voltage, nevertheless since the dc-link capacitance has much longer time constant with the control bandwidth lower than 100 Hz, the influence of dc-link voltage control on the HFR can be neglected. Besides, the grid synchronization is designed with the similar dynamic characteristic as the dc-link voltage control, which can also be neglected.

Thus, Fig. 2(a) and (b) can be merged as shown in Fig. 3. The GSC current closed-loop control is modeled as one voltage source $i^*_{\rm Lf}G_c(s-j\omega_0)G_d(s-j\omega_0)$ and one impedance $Z_{\rm GSC} = G_c(s-j\omega_0)G_d(s-j\omega_0)$ in series, as shown in the blue bracket in Fig. 3.

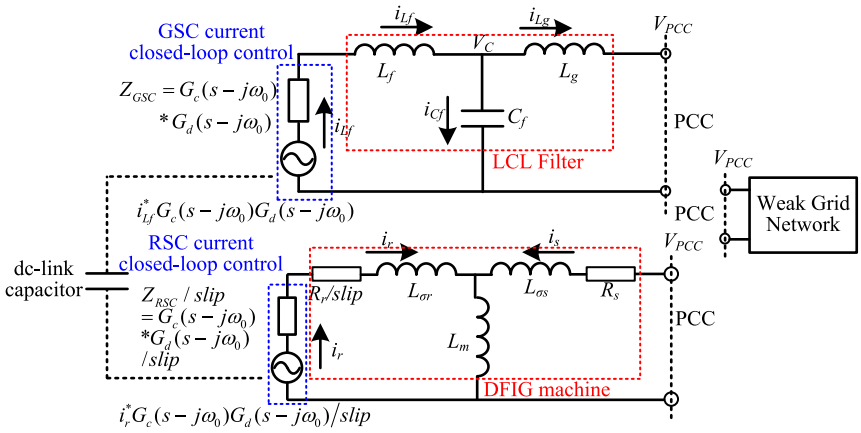

Fig. 6. Equivalent circuit of DFIG system and weak grid network.

Then, the impedance of GSC and LCL filter seen from the PCC can be obtained by setting the voltage source to zero, and the impedance of GSC and LCL filter Z_G can be presented as follows:

$$Z_G = \frac{Z_{Cf}\left(Z_{\mathrm{Lf}} + Z_{\mathrm{GSC}}\right) + Z_{\mathrm{Lg}}\left(Z_{\mathrm{Lf}} + Z_{\mathrm{GSC}}\right) + Z_{Cf}Z_{\mathrm{Lg}}}{Z_{Cf} + \left(Z_{\mathrm{Lf}} + Z_{\mathrm{GSC}}\right)} \tag{2}$$

where $Z_{\mathrm{GSC}} = G_c(s-j\omega_0)G_d(s-j\omega_0)$, $Z_{Cf} = 1/sC_f$, $Z_{\mathrm{Lf}} = sL_f$, and $Z_{\mathrm{Lg}} = sL_g$.

C. RSC and Machine Impedance Modeling

Fig. 4 shows the circuit and control diagrams of RSC and induction machine. Since the rotor current control and output voltage are both presented in the rotor reference frame, they need to be transformed into the stationary frame by the slip angular speed expressed as [9]–[11]

$$\mathrm{slip} = (s - j\omega_r)/s \tag{3}$$

Similarly to the modeling of GSC with an LCL filter, the rotor current control output voltage can be represented as the following according to Fig. 4(b)

$$V_{\mathrm{or}}(s-j\omega_0) = \left(i_r^* - i_r\right)G_c(s-j\omega_0)G_d(s-j\omega_0) \tag{4}$$

where $G_c(s-j\omega_0)$ is the PI current controller containing proportional part K_{prsc} and integral part $K_{\mathrm{irsc}}/(s-j\omega_0)$, the parameters of K_{prsc} and K_{irsc} can be found in Table I.

Then, by merging Fig. 4(a) and (b), the equivalent circuit of RSC and DFIG machine can be obtained as shown in Fig. 5.

Then, the impedance of RSC and DFIG machine seen from the PCC can be obtained by setting the rotor control voltage source to zero, and the impedance of RSC and DFIG machine Z_{SR} can be presented as follows:

$$Z_{\mathrm{SR}} = \frac{Z_{\mathrm{Lm}}H + \left(R_s + Z_{L\sigma s}\right)H + Z_{\mathrm{Lm}}\left(R_s + Z_{L\sigma s}\right)}{Z_{\mathrm{Lm}} + H} \tag{5}$$

where, $H = (R_r + Z_{\mathrm{RSC}})/slip + Z_{L\sigma r}$; $Z_{\mathrm{RSC}} = G_c(s-j\omega_0)G_d(s-j\omega_0)$; $Z_{\mathrm{Lm}} = sL_m$; $Z_{L\sigma r} = sL_{\sigma r}$; and $Z_{L\sigma s} = sL_{\sigma s}$.

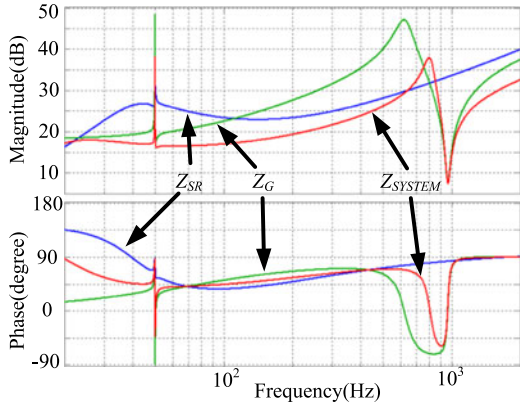

Fig. 7. Bode diagram of the rotor part (RSC and DFIG machine) impedance Z_{SR}, the grid part (GSC and LCL filter) impedance Z_G, and the DFIG system impedance Z_{SYSTEM}.

D. DFIG System Impedance

As analyzed in [9]–[15], the RSC and DFIG machine, together with the GSC and LCL filter, are connected in parallel to the PCC as shown in Fig. 6. As it can be observed, the dc-link capacitor is connected between RSC and GSC, the dc-link voltage is able to remain constant in normal operation circumstance, thus the dc-link capacitor actually has the function of decoupling the control of RSC and GSC. As a result, the RSC and GSC can work independently, and no dc-link coupling between RSC and GSC needs to be taken into consideration in the impedance modeling.

Hence, the grid part (including GSC and LCL filter) Z_G and rotor part (including RSC and DFIG machine) Z_{SR} can be considered as in parallel connection. Based on (2) and (5), the overall DFIG system impedance Z_{SYSTEM} can then be derived as follows:

$$Z_{\mathrm{SYSTEM}} = \frac{Z_G Z_{\mathrm{SR}}}{Z_G + Z_{\mathrm{SR}}}. \tag{6}$$

The Bode diagram of the rotor part (RSC and DFIG machine) impedance Z_{SR}, the grid part (GSC and LCL filter) impedance

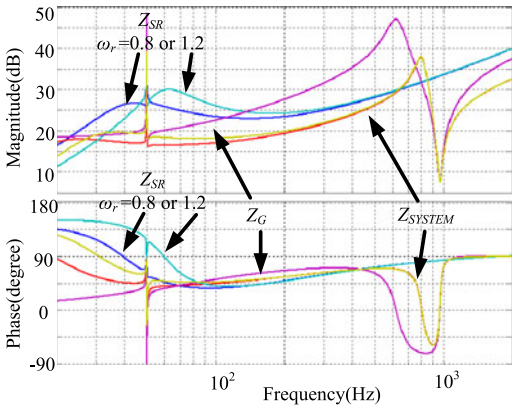

Fig. 8. Bode diagram of the rotor part (RSC and DFIG machine) impedance $Z_{\rm SR}$, the grid part (GSC and LCL filter) impedance Z_G, and the DFIG system impedance $Z_{\rm SYSTEM}$, under different rotor speed (0.8 or 1.2 p.u.).

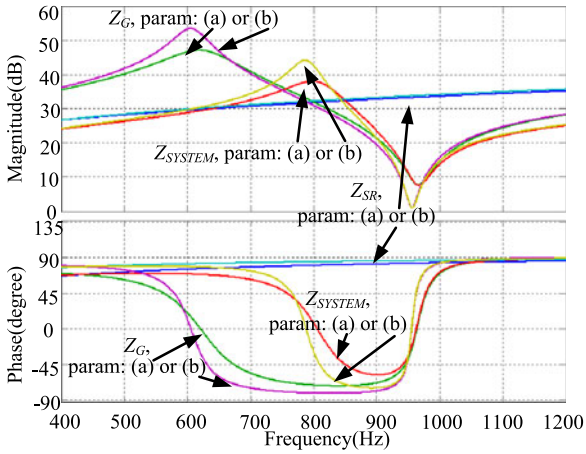

Fig. 9. Bode diagram of RSC and DFIG machine impedance $Z_{\rm SR}$, GSC and LCL filter impedance Z_G and DFIG system impedance $Z_{\rm SYSTEM}$. Under different closed-loop current control PI parameters, (a) $K_{\rm prsc} = K_{\rm pgsc} = 8$, $K_{\rm irsc} = K_{\rm igsc} = 16$; (b) $K_{\rm prsc} = K_{\rm pgsc} = 4$, $K_{\rm irsc} = K_{\rm igsc} = 8$.

Z_G and the DFIG system impedance $Z_{\rm SYSTEM}$ are plotted in Fig. 7, with the parameters given in Table I.

As it can be observed from Fig. 7, within the lower frequency range, both $Z_{\rm SR}$ and Z_G have a high peak at 50 Hz due to the integral part of PI controller rotated from synchronous frame to stationary frame, thus the DFIG system impedance $Z_{\rm SYSTEM}$ also has a high peak at 50 Hz.

As for the higher frequency range (e.g., above 500 Hz), the $Z_{\rm SR}$ behaves as an inductive impedance, having the phase response close to 90°. While for the Z_G, the magnitude response has one peak around 620 Hz and one concave around 966 Hz caused by the LCL filter. More importantly, it needs to be pointed out that the phase response of $Z_{\rm G}$ from 620 and 966 Hz are capacitive below 0°, which is quite different from $Z_{\rm SR}$.

The DFIG system impedance $Z_{\rm SYSTEM}$ has a similar magnitude and phase response as the Z_G. However, due to the involvement of $Z_{\rm SR}$, the $Z_{\rm SYSTEM}$ magnitude peak shifts from 620 to 803 Hz, and the phase response from 803 to 966 Hz is also lifted up, which is helpful to avoid the series HFR (will be explained in following sections).

As reported in [12], the DFIG SSR frequency is partially determined by the rotor speed, and the SSR is more prone to occur with lower rotor speed. Thus, it needs to be studied whether the rotor speed may influence the DFIG system impedance at higher frequency range. Fig. 8 plots the Bode diagrams of $Z_{\rm SR}$, Z_G and $Z_{\rm SYSTEM}$ under different rotor speeds, i.e., 0.8 or 1.2 p.u. It can be seen that the rotor speed variation only affects the impedance of $Z_{\rm SR}$ at the lower frequency range, while the Z_G and $Z_{\rm SYSTEM}$ remains the same at the higher frequency. Thus, it can be concluded that the rotor speed variation is relatively irrelevant to the DFIG system impedance shape at higher frequency range.

Furthermore, according to the impedance expression given in (2), (5), and (6), once the DFIG system is settled, the only adjustable parameters in the impedance are RSC and GSC PI controller parameters. Thus, it is essential to study the influence of RSC and GSC PI controller parameters on the impedance characteristic. As shown in Fig. 9 that depicts the impedance under the different PI controller parameters: 1) $K_{\rm prsc} = K_{\rm pgsc} = 8$, $K_{\rm irsc} = K_{\rm igsc} = 16$; and 2) $K_{\rm prsc} = K_{\rm pgsc} = 4$, $K_{\rm irsc} = K_{\rm igsc} = 8$, the $Z_{\rm SR}$ remains unchanged, while Z_G changes significantly, that is, larger PI controller parameters help to suppress the peak of Z_G magnitude response and to lift up the concave of Z_G magnitude response. Most importantly, the Z_G phase response between 600 and 950 Hz also increases, thus resulting in the phase response of system impedance $Z_{\rm SYSTEM}$ to increase from $-74.9°$ to $-58.7°$ at 900 Hz, which helps to avoid series HFR as it will be illustrated in following.

III. Series HFR Between DFIG System and Weak Network

As mentioned in the introduction, there are three kinds of weak grid network configurations that require investigations for series HFRs between the DFIG system and weak network.

In the following discussion, it is assumed that the DFIG system parameters remain unchanged, thus the DFIG system impedance remains constant. On the other hand, the network impedance may vary due to the different compensation level or other distributed generation unit/load connected to the network. The stable operation range (i.e., no occurrence of series HFR), critical but still stable operation range, as well as the series HFR range will be discussed.

A. Network Impedance of RL in Series and the Resonance Analysis

As the most common type of weak grid network, the network configuration of a resistor and an inductor in series is widely adopted in previous works [16], [18].

The impedance of the series RL network can be presented as follows:

$$Z_{\rm NET\_RL} = sL_{\rm NET} + R_{\rm NET} \tag{7}$$

where $L_{\rm NET}$ is the network inductance, $R_{\rm NET}$ is network resistance.

Based on the knowledge of electric circuit principle, it is clear that the resonance will happen if the DFIG impedance and weak network impedance have same magnitude response

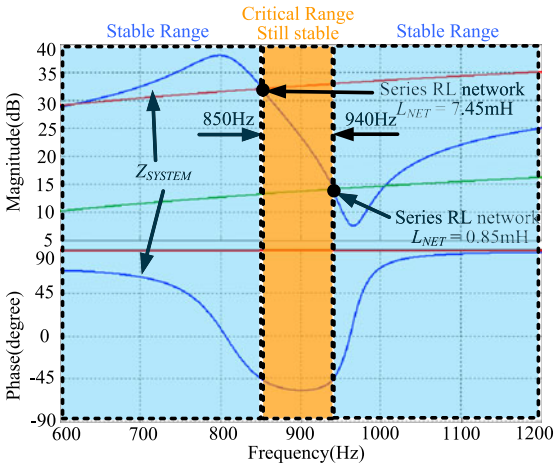

Fig. 10. Bode diagram of DFIG system impedance and series RL network impedance with different L_{NET} (0.85 or 7.45 mH), $R_{\mathrm{NET}} = 3$ mΩ.

(i.e., the magnitude response intersection point) but the opposite phase response (i.e., phase response difference of 180°).

Fig. 10 shows the Bode diagram of series RL network and DFIG system impedance. It can be seen that the series RL network impedance magnitude response will rise up when the network inductance L_{NET} becomes larger. Obviously, there is always one magnitude intersection point between the RL network and the DFIG system. If this intersection point is located between the frequency from 850 to 940 Hz (the orange block noted as Critical but Still Stable Range), then the phase difference will be larger than 135°, that is, 149° for the worst case at 900 Hz, indicating that the series HFR is less likely to occur between the DFIG system and the RL network due to the phase margin larger than 31° (180° - 149°), and the DFIG system is still able to operate stable.

As it can be calculated according to (7), the largest inductance corresponds to the lower limit of the critical range of 850 Hz is 7.45 mH, and the smallest corresponds to the upper limit of the critical range of 940 Hz is 0.85 mH. Thus, it can be found out that under specific DFIG system impedance with the parameters given in Table I, the inductance of the series RL network should be smaller than 0.85 mH or larger than 7.45 mH in order to eliminate the possibility of series HFR between the DFIG system and the series RL network.

Besides, it should also be noted that even there exists a magnitude intersection point at the left or right side of the critical range (in blue), but the phase response difference is much smaller than 135° at this intersection frequency, indicating a sufficiently large phase margin, thus no series HFR will happen.

B. Network Impedance of RLC in Series

Besides the case of the series RL network aforementioned, it is also likely for the network to behave as a series RLC network (series compensated weak network), which has been adopted in [9]–[15].

However, it should be noted that, for the case of series RLC network, the parameters of the inductance L_{NET} and capacitance C_{NET} determine that the RLC network will behave as a RL network at the higher frequency range due to the comparatively large series capacitance C_{NET}. For instance, in [10], the network series L_{NET} is 6.3 μH, the network series capacitor C_{NET} is 2 F.

Therefore, in respect of the series HFR, the case of series RLC network will have the same results as that of series RL network in Fig. 10, thus no further discussion will be repeated here for the sake of simplicity.

C. Network Impedance of Series RL and Shunt C

As another popular weak grid network configuration, the series RL + shunt C network (parallel compensated weak network) requires serious investigation concerning the series HFR.

The impedance of series RL + shunt C network can be presented as follows:

$$Z_{\mathrm{NET\_}RL\_C} = \frac{(sL_{\mathrm{NET}} + R_{\mathrm{NET}})\frac{1}{sC_{\mathrm{NET}}}}{sL_{\mathrm{NET}} + R_{\mathrm{NET}} + \frac{1}{sC_{\mathrm{NET}}}} \tag{8}$$

where C_{NET} is the network shunt capacitor.

Unlike the case of series RL network whose impedance shape looks like a straight line shown in Fig. 10, the impedance of series RL + shunt C network has a peak due to the L_{NET} and C_{NET}, resulting in the resonance analysis more complicated than the case of series RL network.

Rewrite the impedance of series RL + shunt C network as the following based on (8):

$$Z_{\mathrm{NET\_}RL\_C} = \frac{\frac{1}{C_{\mathrm{NET}}}s + \frac{R_{\mathrm{NET}}}{L_{\mathrm{NET}}C_{\mathrm{NET}}}}{s^2 + \frac{R_{\mathrm{NET}}}{L_{\mathrm{NET}}}s + \frac{1}{L_{\mathrm{NET}}C_{\mathrm{NET}}}}. \tag{9}$$

It can be observed from (9) that the network impedance peak is determined by L_{NET} and C_{NET}. In this discussion, it is assumed that the L_{NET} remains constant, while the C_{NET} will vary according to different compensation level or parasite capacitance, thus causing the network impedance peak to shift within certain frequency range.

As shown in Fig. 11, the Bode diagram of DFIG system impedance can be divided into three parts according to its magnitude response, thus the following discussion on the series HFR between the DFIG system and the series RL + shunt C will also be divided into three parts. The DFIG system impedance has a magnitude peak at 800 Hz and magnitude concave at 966 Hz, the corresponding network C_{NET} can be, respectively, calculated as 39 μF at 800 Hz and 27 μF at 966 Hz according to (9) (given the network inductance $L_{\mathrm{NET}} = 1$ mH), and these two frequency points are used to divide the discussion into three parts.

Fig. 11 gives out the Bode diagram of DFIG system impedance and series RL + shunt C network impedance with different C_{NET} (50, 30, 20 μF), $R_{\mathrm{NET}} = 3$ mΩ, $L_{\mathrm{NET}} =$ 1 mH. The three different zones, i.e., lower than 800 Hz, from 800 to 966 Hz, higher than 966 Hz, are divided for the sake of clear illustration. In the following discussion, the network impedance will vary due to the various network capacitance values C_{NET}.

1) Analysis of Zone 1 When C_{NET} is Smaller Than 27μF: Fig. 12 shows the Bode diagram of the DFIG system impedance and series RL + shunt C network impedance with C_{NET} smaller

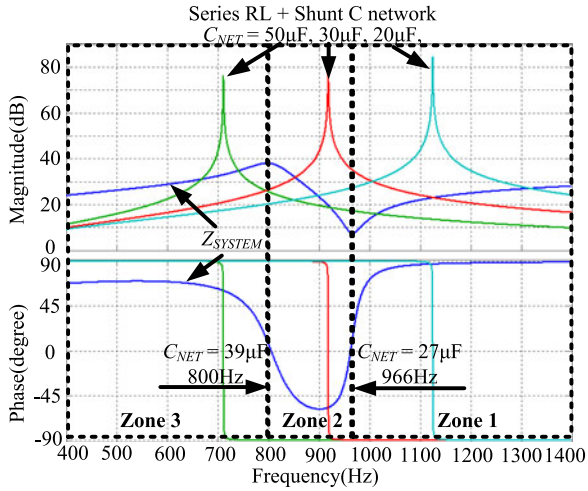

Fig. 11. Bode diagram of DFIG system impedance and series *RL* + shunt C network impedance with different $C_{\rm NET}\,(50, 30, 20\ \mu{\rm F})$, $R_{\rm NET} = 3\ {\rm m}\Omega$, $L_{\rm NET} = 1\ {\rm mH}$.

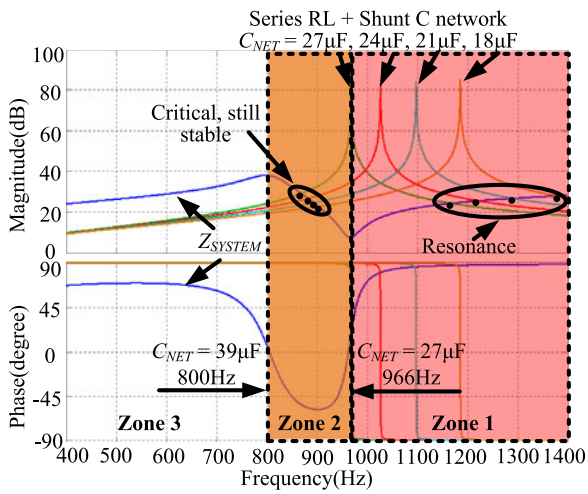

Fig. 12. Bode diagram of DFIG system impedance and series *RL* + shunt C network impedance with $C_{\rm NET}$ smaller than 27 μF (27, 24, 21, 18 μF), $R_{\rm NET} = 3\ {\rm m}\Omega$, $L_{\rm NET} = 1\ {\rm mH}$.

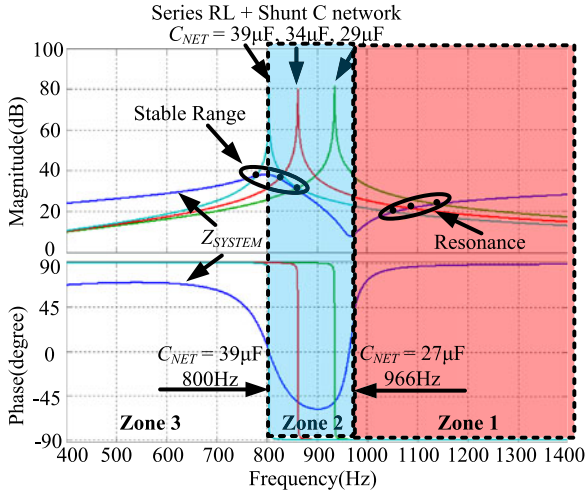

Fig. 13. Bode diagram of DFIG system impedance and series *RL* + shunt C network impedance with $C_{\rm NET}$ between 27 and 39 μF (39, 34, 29 μF), $R_{\rm NET} = 3\ {\rm m}\Omega$, $L_{\rm NET} = 1\ {\rm mH}$.

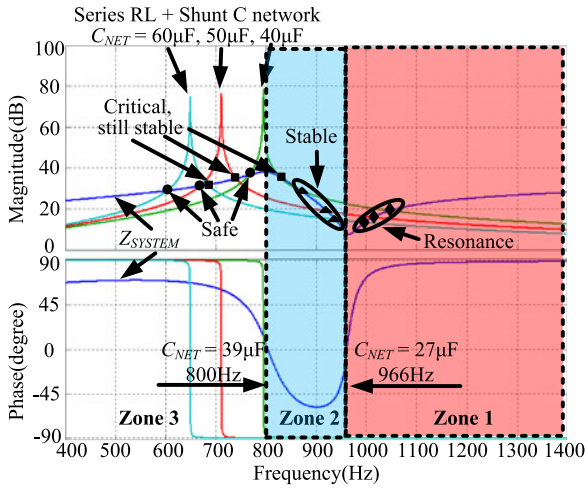

Fig. 14. Bode diagram of DFIG system impedance and series *RL* + shunt C network impedance with $C_{\rm NET}$ larger than 39 μF (40, 50, 60 μF), $R_{\rm NET} = 3\ {\rm m}\Omega$, $L_{\rm NET} = 1\ {\rm mH}$.

than 27 μF (27, 24, 21, 18 μF). As shown clearly, the parallel compensated weak network and the DFIG system have magnitude intersection points in both Zone 2 and Zone 1.

For the intersection points located within Zone 2, the phase differences are from 135° to 149°, which is similar to the situation of series RL network discussed in Section III-A. Thus, for the network shunt capacitor $C_{\rm NET}$ smaller than 27 μF, the resonance frequency from 800 to 966 Hz is less possible to happen, and the DFIG system is still able to work stable due to the acceptable phase margin.

On the contrary, for the intersection points located within Zone 1, the phase difference are always 180° for all four cases of different capacitances, indicating that the series HFR at 1160, 1220, 1290, and 1380 Hz will occur, respectively, for the network shunt capacitor $C_{\rm NET} = 27, 24, 21, 18\ \mu F$.

2) Analysis of Zone 2 When $C_{\rm NET}$ is Between 27μF and 39μF: Fig. 13 shows the Bode diagram of DFIG system impedance and series RL + shunt C network impedance with $C_{\rm NET}$ between 27 and 39 μF (39, 34, 29 μF). Similarly, the magnitude intersection points exist both in Zone 2 and Zone 1.

The intersection points located within Zone 2 have a phase difference smaller than 135°, meaning the phase margin is sufficient to ensure a stable operation of the DFIG system. In contrast, for the intersection points located within Zone 1, the phase difference is very close to 180° for all the four cases of different capacitances, indicating that the series HFR at 1050, 1090, and 1130 Hz is very likely to happen, respectively, for the network shunt capacitor $C_{\rm NET} = 39, 34$ and $29\ \mu F$.

3) Analysis of Zone 3 When $C_{\rm NET}$ is Larger Than 39μF: When the network capacitance $C_{\rm NET}$ is larger than 39 μF, the network impedance has four magnitude intersection points with the DFIG system impedance, which have been noted using dot, square, triangle, and hexagon in Fig. 14.

As it can clearly be observed from Fig. 14, the intersection points at the lowest frequency of 610, 670, and 770 Hz noted

using the dots "·" in Zone 3, have phase difference less than 30°, thus the stable operation can be guaranteed at these low frequencies.

However, as noted using the squares "■" the phase difference at the frequency of 680, 740, and 830 Hz can be as large as 160°, but still is able to work stable due to the acceptable phase margin.

Next, as for the intersection points noted using the triangles ("▲") in Zone 2, the phase difference at 870, 920, and 930 Hz is around 30°, which is similar to the intersection points noted by dot, thus still ensuring the stable operation.

Lastly, for the intersection points noted using "♦," the phase difference is close to 180°, resulting in the high possibility of series HFRs at the frequency of 1000, 1010, and 1050 Hz, respectively.

D. Summary of Series HFR Between the DFIG System and Different Weak Networks

Based on aforesaid discussions, it can be found that, when connected to the series RL and series RLC weak network, the DFIG system is able to work stable without the occurrence of the series HFR due to the acceptable phase margin of around 30° as shown in Fig. 10. Importantly, the acceptable phase margin can be enhanced by adjusting appropriately the PI current closed-loop parameters, which has been validated in [11].

On the other hand, the impedance of the series RL + shunt C weak network (parallel compensated weak network) will behave in different ways with different shunt capacitance values. However, no matter what value the network shunt capacitor is, the series HFR will always happen at the frequency higher than 1000 Hz for the given parameters, which can be validated by Figs. 12–14, while the lower frequency resonance, i.e., around 700–900 Hz is less likely to occur with an acceptable phase margin.

Thus, in order to achieve stable DFIG system operation without series HFR, the effective DFIG system active damping control strategy needs to be taken into action to mitigate the series HFR. Besides, it is also essential to carefully adjust the PI current closed-loop control parameters to avoid the occurrence of lower frequency resonance (around 700–900 Hz). An active damping control strategy for DFIG system will be investigated further in the future works, while the main contribution of this paper is to theoretically analyze the HFR phenomenon of DFIG system

IV. Parallel HFR Between Rotor Part and Grid Part

Besides the series HFR discussed aforesaid, the parallel HFR between rotor part and grid part of DFIG system is also possible to happen and deserves consideration.

Due to the adoption of capacitor unit C_f in the LCL filter for GSC, the grid part impedance behaves capacitive within certain frequency range, while the rotor part (including RSC and DFIG machine) remains inductive within the entire frequency range, as shown in Fig. 7. Therefore, the parallel HFR occurs if the phase difference between rotor part and grid part is close to 180° at the magnitude intersection frequency point.

Fig. 15 gives out the Bode diagram of the rotor part impedance and the grid part impedance with two groups of different

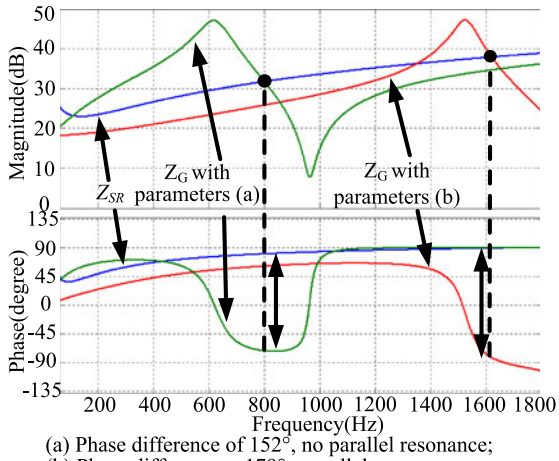

(a) Phase difference of 152°, no parallel resonance;
(b) Phase difference = 179°, parallel resonance occurs.

Fig. 15. Bode diagram of DFIG rotor part impedance $Z_{\rm SR}$ and grid part impedance Z_G with two groups of different LCL filter parameters: (a) $C_f = 6.6\ \mu F, L_f = 11\ \text{mH}, L_g = 7\text{mH}$; (b) $C_f = 6.6\ \mu F, L_f = 2.5\ \text{mH}, L_g = 2\ \text{mH}$.

LCL filter parameters: group (a) $C_f = 6.6\ \mu\text{F}$, $L_f = 11\ \text{mH}$, $L_g = 7\ \text{mH}$; and group (b) $C_f = 6.6\ \mu F$, $L_f = 2.5\ \text{mH}$, $L_g = 2\ \text{mH}$. As it can be seen, when the parameter group (a) is applied for the LCL filter, the magnitude intersection point of DFIG rotor part $Z_{\rm SR}$ and grid part Z_G locates at 800 Hz, and the phase difference is around 152°, thus no parallel resonance will occur, and the DFIG system can work stable on its own. On the other hand, when the parameter group (b) is employed for the LCL filter, the magnitude intersection point moves to 1655 Hz, and the phase difference becomes much larger of 179°, thus the parallel HFR will occur as a consequence.

Based on this result, it is easy to find that the parallel HFR is mainly determined by the grid part impedance character, and more accurately by the LCL filter. Therefore, it can be concluded that the parallel HFR within the interior of DFIG system is sensitive to the LCL filter parameters, and the appropriate design of LCL filter is essential to guarantee the stable operation of DFIG system.

Importantly, one critical fact about the parallel HFR is that, for a well-functioned DFIG-based wind power generation system, the LCL filter must have been carefully designed in order to make the entire DFIG system operate normally and avoid the parallel HFR, therefore the aforementioned parallel HFR between the rotor part and grid part is only possible in the theoretical analysis, but is less likely to happen in the practical case. Hence, it is not necessary to provide experiment validations for the parallel HFR in Section V, but will be under further investigation in the future research work.

V. Experimental Validation

A. Experimental setup

In order to validate the above analysis on the DFIG system impedance modeling and the corresponding series HFR, a downscaled 7.5-kW test rig is built up and shown in Fig. 16. The DFIG system parameters can be found in Table I. The DFIG is

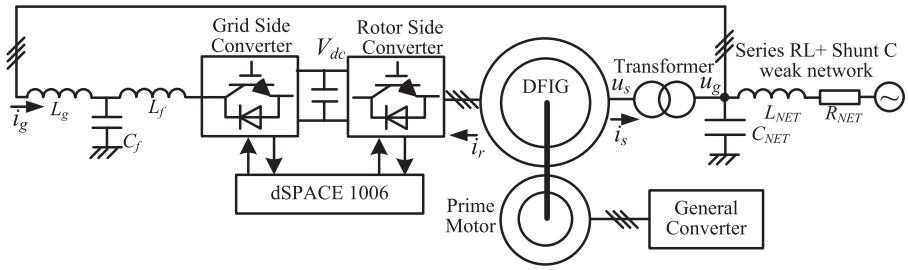

Fig. 16. Setup of a 7.5-kW DFIG system test rig.

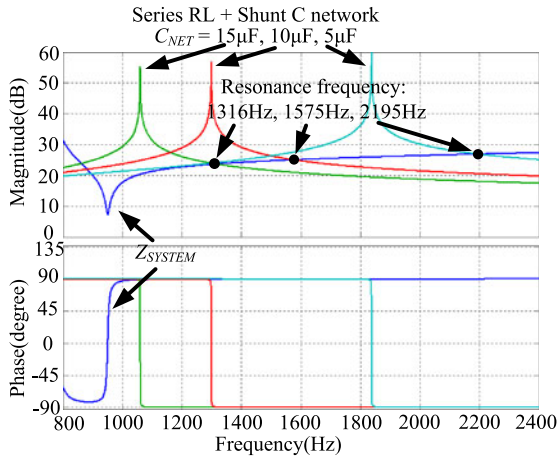

Fig. 17. Bode diagram of DFIG system impedance and series *RL* + shunt C network impedance with $C_{\rm NET} = 15, 10, 5\mu$F, $R_{\rm NET} = 3\ \Omega$, $L_{\rm NET} = 1.5$ mH.

externally driven by a prime motor, and two 5.5-kW Danfoss motor drives are used for the GSC and the RSC, both of which are controlled with dSPACE 1006 control system. The rotor speed is set to 1200 r/min (0.8 p.u.), with the synchronous speed of 1500 r/min (1.0 p.u.). For the purpose of preventing grid connection inrush and inner system current circulation, a transformer is connected between DFIG stator winding and PCC, but it does not change the voltage level between primary and secondary sides. The dc-link voltage is 650 V. The DFIG stator output active and reactive power is 5 kW and 0 Var. The AD sampling and switching frequency of both converters is 10 and 5 kHz, respectively.

The experiment validation is conducted under weak network parameters of $R_{\rm NET} = 3\ \Omega$, $L_{\rm NET} = 1.5$ mH, $C_{\rm NET} = 15,\ 10,\ 5\ \mu$F. The Bode diagrams of these weak grid impedance and DFIG system have been plotted in Fig. 17. As it can be seen, the theoretical analysis shows that the series HFR of 1316, 1575 and 2195 Hz will occur when the shunt capacitance $C_{\rm NET}$ is chosen as 15, 10, and 5 μF, respectively, these results are listed in Table II.

B. Experimental results

Fig. 18 shows the experimental results when no shunt capacitor is connected to the weak network impedance. As it can be seen, the DFIG system is able to maintain satisfactory operation without HFR, all sinusoidal stator/grid voltage and output stator current and grid side current can be observed, which verifies the theoretical analysis conducted in Fig. 10, where the series RL network is considered.

TABLE II
SERIES HFR ACCORDING TO THEORETICAL ANALYSIS AND EXPERIMENTAL RESULTS

Shunt Capacitor	Theoretical Analysis	Experimental Results	
		Subsynchronous speed 1200 r/min	Supersynchronous speed 1700 r/min
15 μF	1316 Hz	1475 Hz	1470 Hz
10 μF	1575 Hz	1600 Hz	1600 Hz
5 μF	2195 Hz	2250 Hz	2125 Hz

It should be noted that, during the experimental validation process, the prime motor is driven by the general converter which will unfortunately inject high-frequency switching noise to the power grid, as a consequence the u_g in all the experiment results Figs. 18—22 will contain switching noise due to the weak power grid impedance. This switching noise can be filtered out by the transformer leakage inductance, thus the stator voltage $u_{\rm s}$ in all the experiment results do not contain the noise.

Figs. 19–21 show the experimental results when the network shunt capacitors $C_{\rm NET} = 15, 10, 5\ \mu F$ are connected, respectively. It is obvious that the series HFR occurs due to the impedance interaction between the DFIG system and parallel compensated weak network. As a consequence, the series HFR occurs in all the stator/grid voltage, DFIG stator, and rotor current as well as grid side current.

By analyzing the waveform containing series HFRs, it can be found out that when the shunt capacitance becomes smaller, the resonance frequency will become larger, the detailed analysis can be found in Table II. According to Table II, there is a certain frequency mismatch between the theoretical analysis and experimental results, the main reason is that the DFIG machine resistance and inductance parameters, grid network inductance $L_{\rm NET}$ and capacitance $C_{\rm NET}$, as well as the GSC LCL output filter, are all very likely to deviate due to the temperature variation, flux saturation, and also skin effect. Since the frequency mismatch between theoretical analysis and experimental results are within acceptable extent, the series HFR experiment results shown in Figs. 19–21 are able to validate the analysis results of the series HFR due to the impedance interaction between the DFIG system and parallel compensated weak network.

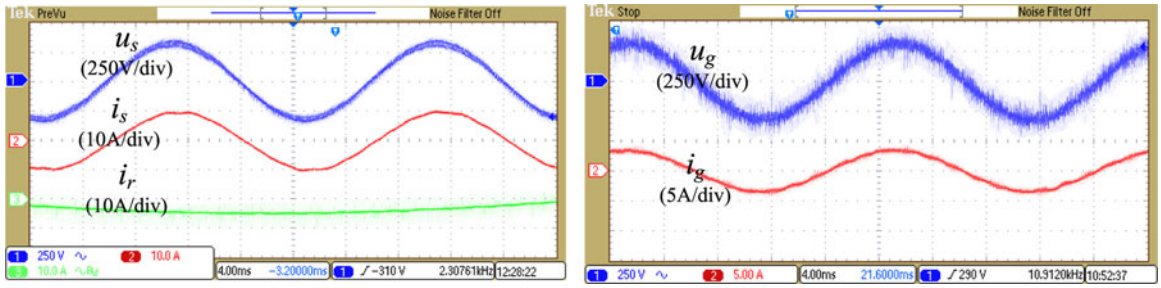

Fig. 18. Experimental result of DFIG system when no shunt capacitor in the weak grid network, $R_{\mathrm{NET}} = 3\ \mathrm{m}\Omega$, $L_{\mathrm{NET}} = 1.5\ \mathrm{mH}$, rotor speed = 1200 r/min (subsynchronous speed).

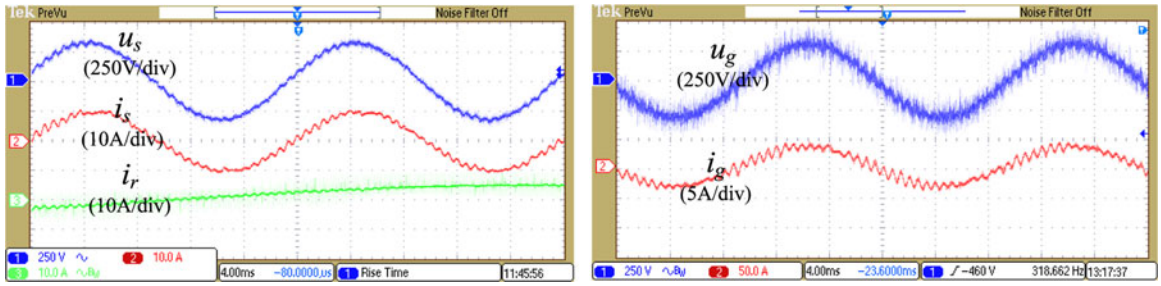

Fig. 19. Experimental result of DFIG system when shunt capacitance $C_{\mathrm{NET}} = 15\ \mu F$ in the weak grid network, $R_{\mathrm{NET}} = 3\ \mathrm{m}\Omega$, $L_{\mathrm{NET}} = 1.5\ \mathrm{mH}$, rotor speed = 1200 r/min (subsynchronous speed).

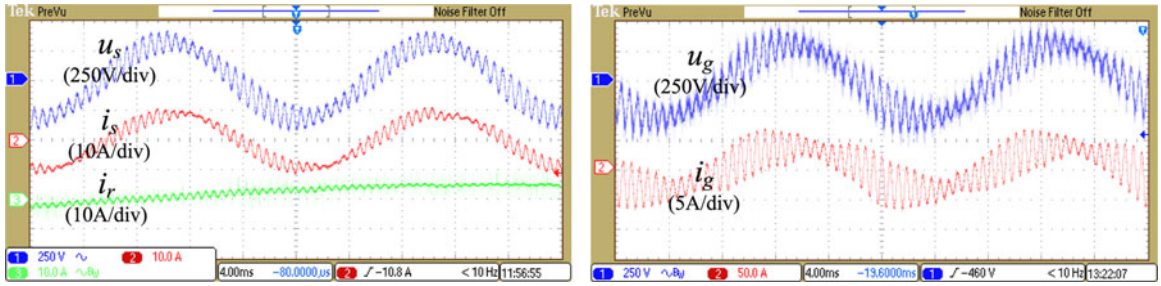

Fig. 20. Experimental result of DFIG system when shunt capacitance $C_{\mathrm{NET}} = 10\ \mu\mathrm{F}$ in the weak grid network, $R_{\mathrm{NET}} = 3\ \mathrm{m}\Omega$, $L_{\mathrm{NET}} = 1.5\ \mathrm{mH}$, rotor speed = 1200 r/min (subsynchronous speed).

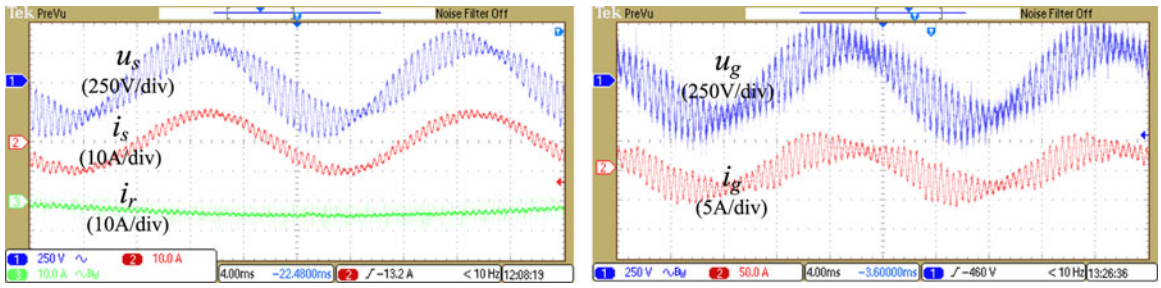

Fig. 21. Experimental result of DFIG system when shunt capacitance $C_{\mathrm{NET}} = 5\ \mu\mathrm{F}$ in the weak grid network, $R_{\mathrm{NET}} = 3\ \mathrm{m}\Omega$, $L_{\mathrm{NET}} = 1.5\ \mathrm{mH}$, rotor speed = 1200 r/min (sub synchronous speed).

In order to validate the influence of DFIG rotor speed on the HFR frequency, the experiments under DFIG rotor super synchronous speed of 1700 r/min are also conducted as shown in Figs. 22–24. As it is shown in Fig. 22, when the network shunt capacitance $C_{\mathrm{NET}} = 15\ \mu\mathrm{F}$, and the rotor speed is 1700 r/min, the HFR frequency is 1470 Hz, this result is very close to Fig. 19, where the experiment result of $C_{\mathrm{NET}} = 15\ \mu\mathrm{F}$ and the rotor speed = 1200 r/min. Similar experiment results can be observed by comparing Fig. 23 (when $C_{\mathrm{NET}} = 10\ \mu\mathrm{F}$ and the rotor speed = 1700 r/min) and Fig. 20 (when $C_{\mathrm{NET}} = 10\ \mu\mathrm{F}$ and the rotor speed = 1200 r/min), i.e., the resonance frequency of 1600 Hz occurs for both cases. Also, by comparing Fig. 24

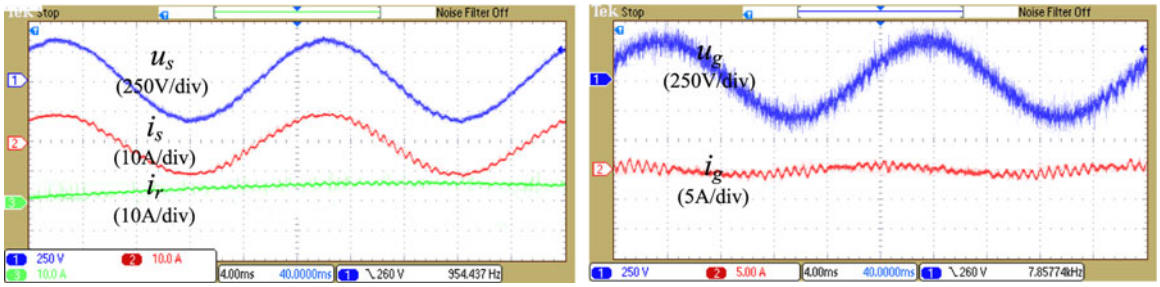

Fig. 22. Experimental result of DFIG system when shunt capacitance $C_{\mathrm{NET}} = 15\ \mu\mathrm{F}$ in the weak grid network, $R_{\mathrm{NET}} = 3\ \mathrm{m}\Omega$, $L_{\mathrm{NET}} = 1.5\ \mathrm{mH}$, rotor speed = 1700 r/min (supersynchronous speed).

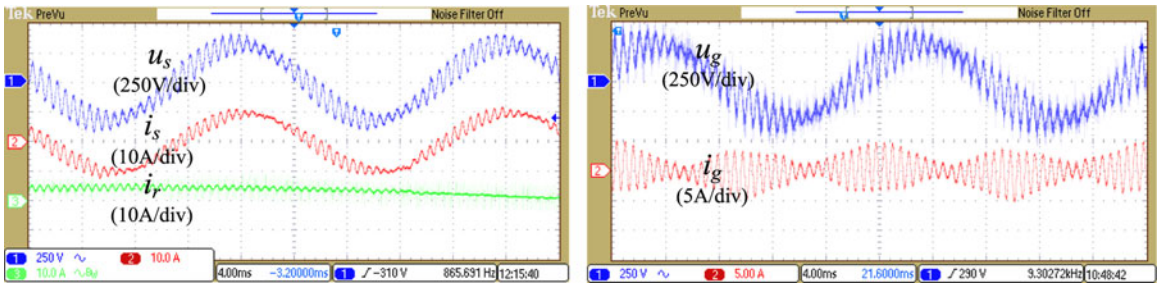

Fig. 23. Experimental result of DFIG system when shunt capacitance $C_{\mathrm{NET}} = 10\ \mu\mathrm{F}$ in the weak grid network, $R_{\mathrm{NET}} = 3\ \mathrm{m}\Omega$, $L_{\mathrm{NET}} = 1.5\ \mathrm{mH}$, rotor speed = 1700 r/min (supersynchronous speed).

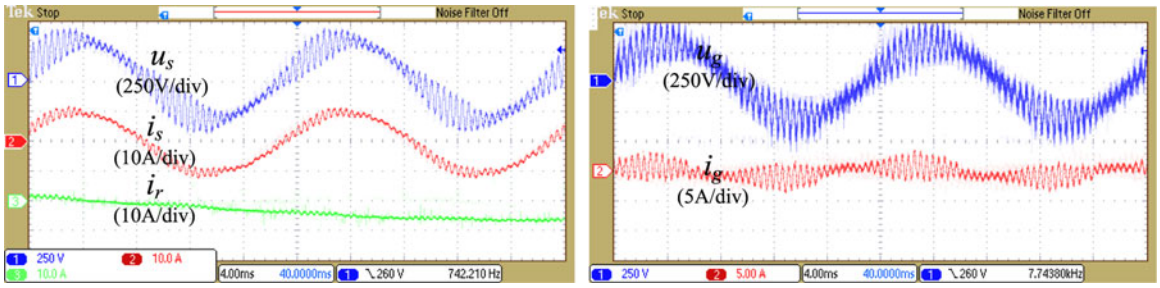

Fig. 24. Experimental result of DFIG system when shunt capacitance $C_{\mathrm{NET}} = 5\ \mu\mathrm{F}$ in the weak grid network, $R_{\mathrm{NET}} = 3\ \mathrm{m}\Omega$, $L_{\mathrm{NET}} = 1.5\ \mathrm{mH}$, rotor speed = 1700 r/min (supersynchronous speed).

(when $C_{\mathrm{NET}} = 5\ \mu\mathrm{F}$ and the rotor speed = 1700 r/min) and Fig. 21 (when $C_{\mathrm{NET}} = 5\ \mu\mathrm{F}$ and the rotor speed = 1200 r/min), it can be found out that the resonance frequency is 2125 and 2250 Hz for each case, respectively. All these experimental analysis data is available in Table II. Thus, based on aforesaid experimental results and analysis data, the conclusion obtained from Fig. 8, i.e., the rotor speed is relatively irrelevant to the series HFR, can be verified.

VI. Conclusion

This paper has focused on the theoretical analysis of the DFIG system series/parallel HFR phenomenon when operating under three alternative weak network configurations. The frequency of the resonance has been theoretically estimated based on the impedance modeling of DFIG system and the weak network.

The contributions of this paper are:

1) The impedances of DFIG system, including:
   a) DFIG machine and RSC;
   b) GSC and output LCL filter are built up for the purpose of HFR analysis.
2) Three alternative weak network configurations are analyzed, i.e., series RL weak network, series RLC (series compensated) weak network, series RL + shunt C (parallel compensated) weak network. From the perspective of series HFR, the major focus has been on the series RL + shunt C network.
3) The rotor speed is relatively irrelevant to the series HFR, and a smaller value of $L_{\mathrm{NET}}C_{\mathrm{NET}}$ results in series HFR with higher frequency. Typically, the DFIG system series HFR is always higher than 1 kHz.
4) The parallel HFR between DFIG rotor part and grid part is also analyzed, and is less likely to happen for a well-functioned DFIG based wind power generation system.

An active damping control strategy of the DFIG system series HFR will be investigated and reported in the near future works.

REFERENCES

[1] F. Blaabjerg and K. Ma, "Future on power electronics for wind turbine systems," *IEEE J. Emerg. Sel. Topics Power Electron.*, vol. 1, no. 3, pp. 139–152, Sep. 2013.

[2] G. Iwanski and W. Koczara, "DFIG-based power generation system with ups function for variable-speed applications," *IEEE Trans. Ind. Electron.*, vol. 55, no. 8, pp. 3047–3054, Aug. 2008.

[3] H. Nian, P. Cheng, and Z. Q. Zhu, "Independent operation of DFIG-based WECS using resonant feedback compensators under unbalanced grid voltage conditions," *IEEE Trans. Power Electron.*, vol. 30, no. 7, pp. 3650–3661, Jul. 2015.

[4] H. Nian, P. Cheng, and Z. Q. Zhu, "Coordinated direct power control of DFIG system without phase-locked loop under unbalanced grid voltage conditions," *IEEE Trans. Power Electron.*, vol. 31, no. 4, pp. 2905–2918, Apr. 2016.

[5] J. Hu, H. Nian, H. Xu, and Y. He, "Dynamic modeling and improved control of DFIG under distorted grid voltage conditions," *IEEE Trans. Energy Convers.*, vol. 26, no. 1, pp. 163–175, Mar. 2011.

[6] H. Xu, J. Hu, and Y. He, "Operation of wind-turbine-driven dfig systems under distorted grid voltage conditions: analysis and experimental validations," *IEEE Trans. Power Electron.*, vol. 27, no. 5, pp. 2354–2366, May 2012.

[7] H. Nian and Y. Song, "Direct power control of doubly fed induction generator under distorted grid voltage," *IEEE Trans. Power Electron.*, vol. 29, no. 2, pp. 894–905, Feb. 2014.

[8] C. Liu, F. Blaabjerg, W. Chen, and D. Xu, "Stator current harmonic control with resonant controller for doubly fed induction generator," *IEEE Trans. Power Electron.*, vol. 27, no. 7, pp. 3207–3220, Jul. 2012.

[9] I. Vieto and J. Sun, "Damping of subsynchronous resonance involving Type-III wind turbines," in *Proc. IEEE 16th Workshop Control Model. Power Electron.* , 2015, pp. 1–8.

[10] I. Vieto and J. Sun, "Small-signal impedance modelling of Type-III wind turbine," in *Proc. Power Energy Soc. General Meet.*, 2015, pp. 1–5.

[11] I. Vieto and J. Sun, "Real-time simulation of subsynchronous resonance in Type-III wind turbines," in *Proc. IEEE 15th Workshop Control Model. Power Electron*, 2014, pp. 1–8.

[12] Z. Miao, "Impedance-model-based SSR analysis for Type 3 wind generator and series-compensated network," *IEEE Trans. Energy Convers.*, vol. 27, no. 4, pp. 984–991, Dec. 2012.

[13] L. Piyasinghe, Z. Miao, J. Khazaei, and L. Fan, "Impedance model-based SSR analysis for TCSC compensated Type-3 wind energy delivery systems," *IEEE Trans. Sustainable Energy*, vol. 6, no. 1, pp. 179–187, Jan. 2015.

[14] L. Fan and Z. Miao, "Nyquist-stability-criterion-based SSR explanation for Type-3 wind generators," *IEEE Trans. Energy Convers.*, vol. 27, no. 3, pp. 807–809, Sep. 2012.

[15] L. Fan and Z. Miao, "Mitigating SSR using DFIG-based wind generation," *IEEE Trans. Sustainable Energy.*, vol. 3, no. 3, pp. 349–358, Jul. 2012.

[16] X. Wang, F. Blaabjerg, and P. C. Loh, "Grid-current-feedback active damping for lcl resonance in grid-connected voltage source converters," *IEEE Trans. Power Electron.*, vol. 31, no. 1, pp. 213–223, Jan. 2016.

[17] X. Wang, Y. Pang, P. C. Loh, and F. Blaabjerg, "A series-LC-filtered active damper with grid disturbance rejection for AC power-electronics-based power systems," *IEEE Trans. Power Electron.*, vol. 30, no. 8, pp. 4037–4041, Aug. 2015.

[18] X. Wang, F. Blaabjerg, and P. C. Loh, "Virtual RC damping of LCL-filtered voltage source converters with extended selective harmonic compensation," *IEEE Trans. Power Electron.*, vol. 30, no. 9, pp. 4726–4737, Sep. 2015.

[19] X. Wang, F. Blaabjerg, and Z. Chen, "Synthesis of variable harmonic impedance in inverter-interfaced distributed generation unit for harmonic damping throughout a distribution network," *IEEE Trans. Ind. Appl.*, vol. 48, no. 4, pp. 1407–1417, Jul./Aug. 2012.

[20] X. Wang, F. Blaabjerg, and Z. Chen, "Autonomous control of inverter-interfaced distributed generation units for harmonic current filtering and resonance damping in an islanded microgrid," *IEEE Trans. Ind. Appl.*, vol. 50, no. 1, pp. 452–461, Jan./Feb. 2014.

[21] X. Wang, F. Blaabjerg, and W. Wu, "Modeling and analysis of harmonic stability in an AC power-electronics-based power system," *IEEE Trans. Power Electron.*, vol. 29, no. 12, pp. 6421–6432, Dec. 2014.

[22] X. Wang, F. Blaabjerg, M. Liserre, Z. Chen, J. He, and Y. Li, "An active damper for stabilizing power-electronics-based AC systems," *IEEE Trans. Power Electron.*, vol. 29, no. 7, pp. 3318–3329, Jul. 2014.

[23] X. Wang, F. Blaabjerg, and M. Liserre, "An active damper to suppress multiple resonances with unknown frequencies," in *Proc. Appl. Power Electron. Conf. Expo.*, 2014, pp. 2184–2194.

[24] X. Wang, Y. Li, F. Blaabjerg, and P. C. Loh, "Virtual-impedance-based control for voltage-source and current-source converters," *IEEE Trans. Power Electron.*, vol. 30, no. 12, pp. 7019–7037, Dec. 2015.

[25] C. Wan, M. Huang, C. K. Tse, and X. Ruan, "Effects of interaction of power converters coupled via power grid: A design-oriented study," *IEEE Trans. Power Electron.*, vol. 30, no. 7, pp. 3589–3600, Jul. 2015.

[26] X. Wang, C. Bao, X. Ruan, W. Li, and D. Pan, "Design considerations of digitally controlled LCL-filtered inverter with capacitor current-feedback active damping," *IEEE J. Emerg. Sel. Topics Power Electron.*, vol. 2, no. 4, pp. 972–984, Dec. 2014.

[27] L. Harnefors, X. Wang, A. G. Yepes, and F. Blaabjerg, "Passivity-Based Stability Assessment of Grid-Connected VSCs-An Overview," *IEEE J. Emerg. Sel. Topics Power Electron.*, vol. 4, no. 1, pp. 116-125, Mar. 2016.

[28] C. Bao *et al.*, "Step-by-step controller design for LCL-Type grid-connected inverter with capacitor–current-feedback active-damping," *IEEE Trans. Power Electron.*, vol. 29, no. 3, pp. 1239–1253, Mar. 2014.

[29] D. Pan, X. Ruan, C. Bao, W. Li, and X. Wang, "Capacitor-current-feedback active damping with reduced computation delay for improving robustness of LCL-Type grid-connected inverter," *IEEE Trans. Power Electron.*, vol. 29, no. 7, pp. 3414–3427, Jul. 2014.

[30] D. Pan, X. Ruan, C. Bao, W. Li, and X. Wang, "Optimized controller design for LCL-Type grid-connected inverter to achieve high robustness against grid-impedance variation," *IEEE Trans. Ind. Electron.*, vol. 62, no. 3, pp. 1537–1547, Mar. 2015.

[31] D. Yang, X. Ruan, and H. Wu, "Impedance shaping of the grid-connected inverter with LCL filter to improve its adaptability to the weak grid condition," *IEEE Trans. Power Electron.*, vol. 29, no. 11, pp. 5795–5805, Nov. 2014.

[32] V. Yaramasu, B. Wu, P. C. Sen, S. Kouro, and M. Narimani, "High-power wind energy conversion systems: State-of-the-art and emerging technologies,"in *Proc.IEEE*, vol. 103, no. 5, pp. 740–788, May 2015.

[33] Z. Chen, J. M. Guerrero, and F. Blaabjerg, "A review of the state of the art of power electronics for wind Turbines," *IEEE Trans. Power Electron.*, vol. 24, no. 8, pp. 1859–1875, Aug. 2009.

[34] X. Wang, F. Blaabjerg, and P. C. Loh, "Proportional derivative based stabilizing control of paralleled grid converters with cables in renewable power plants," in *Proc. Energy Conversion Congr. Expo.*, 2014, pp. 4917–4924.

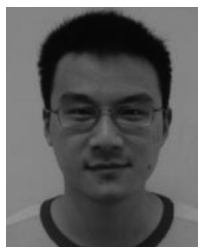

Yipeng Song was born in Hangzhou, China. He received the B.Sc. and Ph.D. degrees both from the College of Electrical Engineering, Zhejiang University, Hangzhou, China, in 2010 and 2015, respectively.

He is currently a Postdoc at the Department of Energy Technology, Aalborg University, Aalborg, Denmark. His current research interests include motor control with power electronics devices in renewable-energy conversion, particularly, the control and operation of doubly fed induction generators for wind power generation.

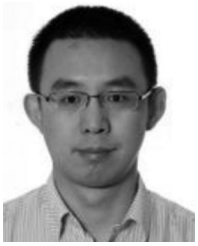

Xiongfei Wang (S'10–M'13) received the B.S. degree from Yanshan University, Qinhuangdao, China, in 2006, the M.S. degree from Harbin Institute of Technology, Harbin, China, in 2008, both in electrical engineering, and the Ph.D. degree from Aalborg University, Aalborg, Denmark, in 2013.

Since 2009, he has been with the Aalborg University, Aalborg, Denmark, where he is currently an Assistant Professor in the Department of Energy Technology. His research interests include modeling and control of grid-connected converters, harmonics analysis and control, passive and active filters, and stability of power electronic-based power systems.

He received an IEEE Power Electronics Transactions Prize Paper Award in 2014. He serves as the Associate Editor of the IEEE TRANSACTIONS ON INDUSTRY APPLICATIONS and the Guest Associate Editor of the IEEE JOURNAL OF EMERGING AND SELECTED TOPICS IN POWER ELECTRONICS Special Issue on Distributed Generation.

Frede Blaabjerg (S'86–M'88–SM'97–F'03) was with ABB-Scandia, Randers, Denmark, from 1987 to 1988. From 1988 to 1992, he received the Ph.D. degree with Aalborg University, Aalborg, Denmark.

He became an Assistant Professor in 1992, an Associate Professor in 1996, and a Full Professor of power electronics and drives in 1998. His current research interests include power electronics and its applications such as in wind turbines, PV systems, reliability, harmonics, and adjustable speed drives.

He has received 17 IEEE Prize Paper Awards, the IEEE PELS Distinguished Service Award in 2009, the EPE-PEMC Council Award in 2010, the IEEE William E. Newell Power Electronics Award 2014, and the Villum Kann Rasmussen Research Award 2014. He was an Editor-in-Chief of the IEEE TRANSACTIONS ON POWER ELECTRONICS from 2006 to 2012. He is nominated in 2014 and 2015 by Thomson Reuters to be between the most 250 cited researchers in Engineering in the world.